Specular Reflection Removal for 3D Reconstruction of Tissues using Endoscopy Videos

Muhammad Emaduddin
Department of Computer Science and Engineering
Texas A&M University
College Station, Texas
emaad22@tamu.edu

Tansel Halic
Intuitive Surgical
Peachtree Corners, Georgia
tansel.halic@intusurg.com

Doga Demirel*
Department of Computer Science
Florida Polytechnic University
Lakeland, Florida
ddemirel@floridapoly.edu

Coskun Bayrak
Department of Computer Science
Youngstown State University
Youngstown, OH
cbayrak@ysu.edu

Venkata S. Arikatla
Kitware, Inc.
Carrboro, North Carolina
sree.arikatla@gmail.com

Suvranu De
College of Engineering
Florida A&M University – Florida State University
Tallahassee, Florida
sde@eng.famu.fsu.edu

SoutheastCon 2023 | 978-1-6654-7611-9/23/$31.00 ©2023 IEEE | DOI: 10.1109/SoutheastCon51012.2023.10115137

***Abstract*— Endoscopy is widely employed for diagnostic examination of the interior of organs and body cavities and numerous surgical interventions. Still, the inability to correlate individual 2D images with 3D organ morphology limits its applications, especially in intra-operative planning and navigation, disease physiology, cancer surveillance, etc. As a result, most endoscopy videos, which carry enormous data potential, are used only for real-time guidance and are discarded after collection. We present a complete method for the 3D reconstruction of inner organs that suggests image extraction techniques from endoscopic videos and a novel image pre-processing technique to reconstruct and visualize a 3D model of organs from an endoscopic video. We use advanced computer vision methods and do not require any modifications to the clinical-grade endoscopy hardware. We have also formalized an image acquisition protocol through experimentation with a calibrated test bed. We validate the accuracy and robustness of our reconstruction using a test bed with known ground truth. Our method can significantly contribute to endoscopy-based diagnostic and surgical procedures using comprehensive tissue and tumor 3D visualization.**

Keywords*— *Endoscopy, 3D reconstruction, 3D mapping, specular reflection removal, tissue, GI tract

I. Introduction

This paper addresses the problem of estimating a 3D reconstruction using images retrieved using endoscopic video images. Endoscopy and its surgery-specific derivatives, i.e., diagnostic imaging, surgical guidance, and cancer surveillance, all use 2D imaging to visualize an internal tissue or organ's true medical character and profile. Although endoscopy videos contain extensive information, the unwieldy 2D view currently leads to clinical practices of condensing lengthy video data into a few still images, along with brief notes or drawings regarding the locations and appearance of suspicious tumors and scars during diagnosis. In surgery, the 2D view augments extra complexity to identify the anatomical landmarks, lesion detection, operative complications, etc. Thus, a comprehensive representation of the endoscopy data that enables a straightforward and rapid review of a 3D reconstruction resulting from a Multi-view Geometry based photogrammetry algorithm could better support the clinical decision-making process. In this paper, we focus on generating 3D models of the interior of organs, such as the gastrointestinal (GI) tract, which is an important and clinically significant application. We emphasize our method's ability to reconstruct an accurate and clinically useful tumor model within the GI tract. We also evaluate the accuracy of reconstruction and dataset collection parameters for the upper GI tract using a custom-built test bed with known dimensions. Although not anatomically accurate, the employed test bed represented the inner stomach and inner esophagus while keeping certain significant dimensions anatomically correct. Such an approach lets us better quantify the accuracy of our proposed method

Several works attempt to produce accurate 3D reconstructions via images of organs, but fewer studies focus on the inner 3D reconstruction in the presence of specular highlights. Our method aims to capture the 3D organ shape and appearance while depicting clinically significant regions and sub-regions of organs. The ultimate goal of this work is to enable end-users (e.g., physicians and surgeons) to localize individual organ regions to anatomical locations in the organ despite the presence of specular highlights in the input image set. However, some authors have found success at reproducing organ regions such as 3D tumors, with relative accuracy, yet these techniques employed additional sensor and environmental overhead in clinical terms, i.e., stereo-cameras [4], cameras or light sources with polar lenses [5], structured light illumination projectors [11], time of flight cameras [12] and optical position trackers [13]. Our method uses various pre-processing techniques to limit the sources of 3D reconstruction errors in the input endoscopic videos. Such sources of errors include motion blur, specular highlights, and illumination variance. It must be mentioned here

that the endoscopic light source is mounted as a part of the endoscope, which illuminates surfaces in the direction of the endoscope. Therefore, images captured at changed perspectives will have varying lighting conditions concerning the surrounding geometry and obscured surfaces around the endoscope. The varying lighting conditions make feature detection and matching less reliable. Robust feature matching in the presence of artifacts such as specular highlights is hard to achieve as these serve to corrupt the description of features and even cause inaccuracies or failure in 3D reconstruction. Simultaneous localization and mapping (SLAM) and structure from motion (SfM) algorithms work well on a small number of images, removing the need to solve the problem of matching a feature pair from distant camera perspectives. In our case, such feature pairs need to be matched since the interior of organs is observed at close range; thus, all features belonging to an organ region are not likely to fall in a single camera frame.

After outlining the previous work conducted in the domain of image-based 3D reconstruction in section II, section III illustrates the test-bed constitution and employed sensor specifications for dataset collection. Section IV details our proposed method by describing (a) endoscopic video parsing & in-focus image extraction, (b) avoiding fatty tissue removal, (c) adapted specular highlights removal, and (d) random patch reconstruction technique. Section V outlines the experiments' results and briefly discusses the proposed method's utility and shortcomings for varying scenarios. The performance of the proposed method is evaluated based on a comparison with ground truth. Detailed results are presented by comparing the method outputs to similar results generated by state-of-art methods in the relevant domain.

II. Literature Review

Endoscopy is a common technique in various medical fields, like lesion diagnosis in hollow organs or mini-invasive surgery. Due to its prevalence and importance in the clinical workflow leading to a diagnosis, many have attempted to enrich the conclusions drawn from endoscopy datasets. 3D reconstruction of organ cavities or lesions has been on the front lines of research in this context. The approaches for 3D reconstruction that utilize standard clinical hardware with almost no constraints on data collection over the last decade are summarized well by articles [14, 15]. Nonetheless, the challenges faced due to illumination variance and specular highlights have not yet been addressed explicitly by prior research. While the shape of the body cavity is useful for the localization of organ sub-regions and lesions by the physician, the surface appearance or texture is of more critical importance to the physician than the exact shape (e.g., surface pattern in colorectal tumors). We avoid comparing our approach to reconstruction approaches, which only present the construction of the organ's shape [16, 17] and not the complete 3D reconstruction, including a textured organ model.

Very few works have explicitly addressed the removal of specular highlights and reflections to improve 3D reconstruction accuracy and extraction of viewpoint-independent diffused color components for feature points [1, 6]. These works assume that the feature point's diffused color component will never reach a zero-magnitude due to the scene constraints or the use of a polarization filter. A particular study by Stoyanov et al. [5] emphasizes the reconstruction errors caused by prominent specular highlights caused by surgical instruments but does not offer any resolution technique to rectify these errors. In [17], the authors use a dichromatic model to remove specular reflection from pixels to aid the texture reconstruction. The assumption in this work is that the diffused component of any pixel will never reach zero. Tan et al. [18] propose an in-painting technique for specular highlight removal. Here the diffuse reflection of the specular pixel is determined based on the dichromatic reflection model. It is also assumed that a uniform illuminant color exists within the highlighted region. Although this method can preserve the diffuse shading in the highlighted region with strictly all pixels with non-zero diffused components, issues may arise from discontinuities in surface colors. Approaches such as [19] present elaborate methods to reconstruct organs such as a bladder but do not provide any solution to the specular highlights problem except using a primitive blur filter to reduce specular artifacts.

Yoon et al. [20] claim to remove specular reflections from any stereo image dataset and improve the accuracy of disparity maps even in the presence of specular highlights. This work presents a notion of a specular-free two-band image that provides a specularity-invariant image representation. This representation is a simple pixel-wise computation and effectively removes specular highlights with a small pixel footprint. This algorithm, however, fails in the case of prominent specular highlights. In a recent method presented by Yang et al. [21], an effective specular highlight removal method is proposed, it is based on a key observation that the maximum fraction of the diffuse color component in diffuse local patches in color images changes smoothly. However, this method is again unable to handle zero-magnitude diffuse components as it can only remove specular highlights under a maximum diffuse chromaticity limit.

Our proposed method in this work has novel techniques to eliminate the specularity in the endoscopic video images. In addition, our approach significantly improves Yang et al.'s approach for the specular highlight removal technique [21] and overcomes the problems of eliminating specularity and noise over a region with no diffused component.

III. Test Bed and Dataset Collection

A multipronged investigative strategy was employed to test and evolve the proposed method. Firstly, a test bed was created to target regions of the GI tract as our ultimate goal for tissue reconstruction. The test bed dimensions are shown in figure 1. These dimensions represent cavities in the upper GI tract, including the esophagus (typically 1-inch diameter, 10-14 inches) and the stomach (typically 2 to 3 liters capacity). As actual dimensions of a human male adult's upper GI tract differ from person to person, it was decided to settle on dimensions closest to the average dimensions found in human anatomy and commercially available construction units, i.e., chambers and pipes.

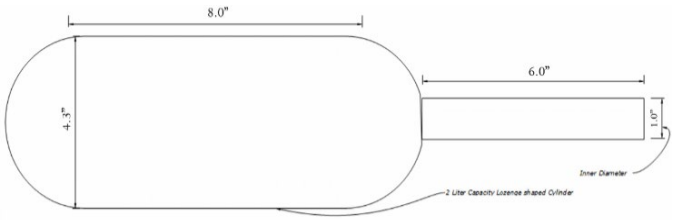

Fig. 1: Upper GI Cavity test bed and dimensions (in inches).

The test bed was primarily used to determine the reconstruction accuracy. The interior of the test bed was painted using random brush strokes to maximize the unique visual features in the image dataset. Only the interior of the test bed was observed using a borescope camera having 640x480 pixel resolution (0.3-megapixel active pixels), 2" to 6" focus range, 60 degrees Field of view (FOV), 1 meter stiff but flexible cord to be used as camera holder. This camera has small dimensions exceeding 0.32" in diameter and 1.84" in length, making it suitable for borescope applications in small cavities.

As the second prong of our strategy, multiple datasets were collected for tissue and tissue-like objects ex-vivo. This was done using a high-resolution camera (4032x3024) with a focus range of 1" to 10", 78-degree FOV and a light source similar to the endoscope light source. The subjects of these datasets were poultry tissue and plum. These objects were chosen explicitly as their reflective characteristics closely match those of cavities associated with the GI tract. There were camera pose constraints applied during the collection of these datasets. As per Figure 2, for an image to be captured, the camera location and orientation must be within certain bounds placed on values 'b' and Ø. These bounds are strictly dictated by the camera's Depth of Field (DoF), represented by blue in the figure, the camera's dimensions, and the cavity's volume. Length 'a' is also strictly bounded between the DoF range. For the particular scenario illustrated in Figure 2 and as per the volume of the stomach cavity, i.e., ~2 liters, and camera DoF, i.e., 1" to 3.5", these ranges turn out to be $2" \leq b \leq 3.5"$ and $Ø \geq 0$. The underlying idea behind these bounds is to maximize the observed surface area, marked red in the figure while maximizing the angle of approach Ø. This strategy ensures the maximum correspondence of visible pixels to the extracted visual features like SIFT. The success of this strategy is validated via the high-quality 3D reconstruction achieved, which is discussed in detail in the results section.

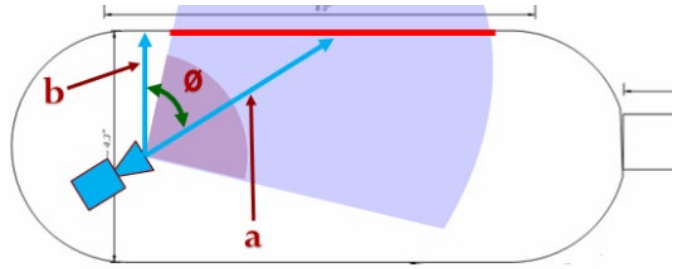

Fig. 2: Length a represents the camera distance to the observed surface. Length b represents the minimum distance of the camera to the observed surface. Ø represents the angle of approach.

The investigative strategy's last element comprises in-vivo endoscope-based dataset collection. Datasets consisting of several hours of endoscopic video were acquired depicting multiple standard clinical procedures. A range of video clips were demarcated keeping in view factors such as (i) the number of focused/non-blurred frames, (ii) the number of focused frames capturing a lesion or a region of interest, (iii) camera pose-variety and inter-pose distance between focused frames and (iv) avoidance of any dynamic objects that render the scene non-static such as instruments or change in cavity walls or lesion structure. We reconstructed a lesion at the proximal antrum region of the stomach to test our method.

IV. Proposed Methodology

The proposed method and some of its own novelties use a previously proposed specular highlight removal technique [21]. While the technique proposed in [21] removes specular noise robustly and reliably in our tissue datasets, it fails to remove specular noise from pixels with zero diffused components. The technique that was employed before involved bilateral filtering with the assumption that the maximum fraction of the diffuse color component, which is commonly known as the maximum diffuse chromaticity in literature, changes smoothly in local patches of color images. A detailed stepwise explanation of the proposed method is given in the next section.

A. Endoscopic Video Parsing and In-focus Image Extraction

This module takes endoscopic video or a pre-saved camera-based image set as input. Its job is to select frames or images that conform to a specific focus criteria and forward these frames to the next module in the processing pipeline. This module initially assesses the motion blur in the images provided by the camera. This is done to determine whether the current frame contains reliable, trackable SIFT features. In case the frame is determined to be non-blurry, the frame is added to a sub-set that will eventually be forwarded to the next module. The motion blur is detected using a weighted average of two detection methods [8, 9]. The first detection method works via convolving the image with a Laplacian operator. The Laplacian operator highlights regions containing rapid intensity changes. The assumption here is that if an image contains high variance, then there is widespread of both edge-like and non-edge-like, representative responses of a normal, in-focus image. But if there is a very low variance, then there is a small spread of responses, indicating fewer edges in the image.

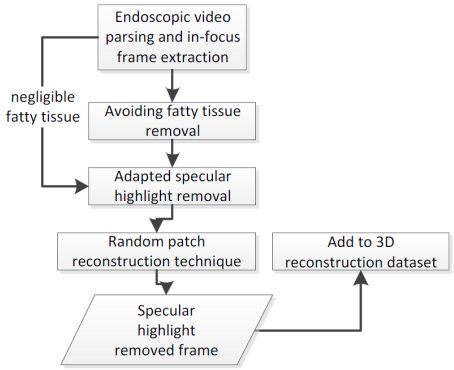

Fig. 3: Method Flow-chart

The Laplacian kernel can be computed using the following expression: x and y represent the 2D kernel row and column indices.

$$LoG(x,y) = \frac{1}{\pi\sigma^4}\left[1 - \frac{x^2+y^2}{2\sigma^2}\right]e^{-\frac{x^2+y^2}{2\sigma^2}} \quad (1)$$

The second blur detection method is based on Normalized Grey Level Variance among image pixels. In this measure, bright and dark pixels have the same influence on the measure. Normalized variance, in this case, compensates for the differences in average image brightness among different images. It is essential to mention here that due to camera orientation towards the inner walls of the cavity and the nature of motion vectors, the images suffer from non-uniform blur. The following expression quantifies the measure term.

$$F_{normvar}(x,y) = \frac{1}{MN\bar{g}}\sum_{M}\sum_{N}[g(x,y) - \bar{g}]^2 \quad (2)$$

A weighted combination of both blur-detection methods was deployed, and a threshold value was determined empirically to classify between blurry and non-blurry frames.

B. Avoiding Fatty Tissue Removal

After passing the motion blur test, the subset of frames is evaluated for the size of the largest fatty tissue. Previously proposed methods [17-20] consider white fatty tissue in our datasets as specular highlights causing unnecessary loss of information. To avoid this problem, fatty tissue is distinguished from specular highlight via a smooth specular continuity constraint. Fatty tissues do not conform to such a constraint; thus, corresponding pixels are left out of the specular highlight removal processing loop. We use the Intensity Logarithmic Differentiation technique defined in [22].

C. Adopted Specular Highlight Removal

The bilateral Filtering based Specular Highlight Removal technique in [21] was adapted to suit our collected datasets. Primary concerns addressed under the proposed adaptation include:

1. Specular highlight removal for light sources creating prominent highlights, i.e., more than 1⁄2 inch in diameter.
2. Partial Estimation of missing information through di-chromatic reflection model.
3. Estimation of missing information, i.e., zero diffused component through random patch reconstruction.

The method is listed stepwise below:

1. Each pixel in the image is divided into diffused and specular reflection components using a bilateral filtering method [21].

2. Divide the original image into three color channels blue (B), green (G), and red (R). Find specular highlight boundaries $b_i \epsilon\ (b_1, b_2, \ldots, b_n)$ for each of the channels based on a grey-level threshold for each channel; $thresh_B$, $thresh_G$, $thresh_R$. We do not include boundaries for fatty tissue segments identified. The illustration in Figure 4 shows the yellow arrows that mark the highlighted patch's boundaries.

Fig. 4: (Right) Yellow arrows mark the boundaries of the highlighted patch. (Left) The peak grey value of the Specular component indicates a specular highlight. Often, there is no diffuse component for pixels where peak values for specular components exist.

3. Now for each pixel that lies within b_i, a color is chosen using a novel random patch reconstruction technique. The chosen color is assigned to $rndcolor$.

4. Use a preference relation to assign a diffused component and a specular component to each pixel having it's specular greater than $thresh_{spec}$ value. These pixels are expected to be part of the specular highlight we wish to remove and will usually have a large specular component. The preference relation is based on the sigmoid function, which helps to smoothly transfer weight from diffused components over to random patch values. The relation is given by

$$wt = \min\left(\frac{1}{(1+e^{-30(spec_{x,y} - thresh_{spec})}}, 1\right) \quad (4)$$

$$img_{x,y}.b = (1 - wt)\left(diffuse_{x,y}.b + spec_{x,y}\right) + wt(rndcolor.b) \quad (5)$$

5. Here $diffuse_{x,y}$ and $spec_{x,y}$ represent the diffused and the specular component of a color pixel. It must be noted here that diffused component consists of .b(blue), .g(green), and .r(red) channels, while the specular component only consists of the single grey-level channel. It must also be noted that equation (5) needs to be written for both green and red channels. Provided we use the convention of assigning float values from 0 to 1 to b, g, r, and grey channels, a resultant function graph representing (5) can be seen in Figure 5.

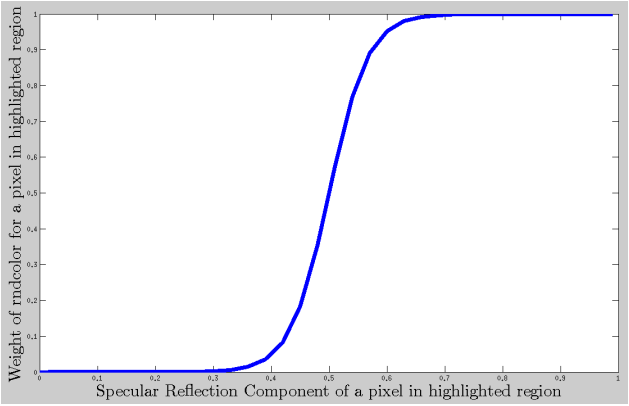

Fig. 5: Function plot representing Eq. 5 where $\boldsymbol{thresh}_{\boldsymbol{spec}}$ value is 0.5. The sigmoid shows the smooth transition from diffused component to $\boldsymbol{rndcolor}$ for a pixel located in the highlighted region.

D. Random Patch Reconstruction Technique

Missing diffused reflection component information due to zero-magnitude diffused components can be estimated through random patch reconstruction. The most apparent benefit of such an approach is that the descriptors of the corresponding local features do not produce a false match between an image pair having a scene overlap. The random patch reconstruction technique comprises of following steps;

1. Select patches of values greater than $thresh_B$, $thresh_G$ and $thresh_R$ for each of the Blue, Green, and Red channels.
2. Calculate the average area of all three patches. Choose the patch with the area closest to the average area. We do this because patches in Blue, Green and Red channels sometimes differ in size by a significant margin. The average patch size is usually representative of the highly specular area.
3. We randomly fill this patch with the color of any patch boundary points that satisfy the criteria in 4.
4. In case a point $pt_{x,y}$ lies between the patch center and boundary point or in its vicinity (dictated by param1), it is randomly allotted the color of the closest points on the patch boundary. This color is allotted to $rndcolor$.
5. To further elaborate, see Figure 6 (Right). This diagram shows that for any gray points, it is evaluated whether the gray point lies between a boundary pixel and a black patch center. This is only true if
   - r1+b1 <= param1*dist(center to boundary pt)
   - r2+b2 <= param1*dist(center to boundary pt)
   - r3+b3 <= param1*dist(center to boundary pt)
   - r4+b4 <= param1*dist(center to boundary pt)

In the scenario given in Figure 6 (right), we see that r4+b4 <= param1*dist (center to boundary pt) is not equal to true. Thus, the gray point, which involves r4 and b4, is not between the patch center and the boundary point in question (orange). In case a point lies between the patch center and the orange boundary point or in its vicinity (dictated by Param1), it is randomly allotted orange, red, or yellow color, i.e., the color of neighbors of orange or its color is allotted to $rndcolor$.

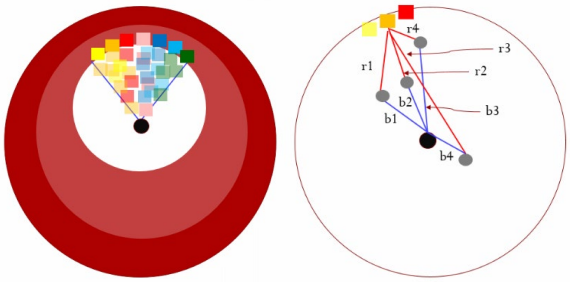

Fig. 6: (Left) Partially filled patch points. Notice how each patch point has a color from a set of patch boundaries closest to it. (Right) It is evaluated whether the grey point lies between a boundary pixel and black patch center for any gray points.

V. Results

Out of many in-vivo and ex-vivo datasets, results for only three are presented here. Detailed results and justification for selecting each dataset set are listed below. The following datasets were processed through the method pipeline, and respective 3D reconstructions were created.

Stomach & Esophagus (Upper GI tract test bed) Dataset: This dataset is chosen to establish an accuracy baseline since ground truth is available. Results are very accurate for highly textured chambers, and the pipe's interior surface was detected as sub-millimeter ridges within the chamber. The model was accurate within ±0.7 mm except for the edges of the model, which were not thoroughly captured. 3D reconstruction results can be seen in Figure 7.

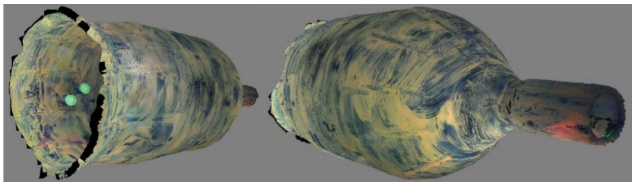

Fig. 7: 3D Reconstruction results for Upper GI tract test bed. Mock tumors (light green) can also be observed in the reconstruction.

Poultry Tissue Dataset: This dataset is chosen as the poultry tissue reflectivity is similar to GI tract walls. The tissue also bears some fat, so it is a good choice for a fatty tissue reconstruction test. The results were accurate from contemporary methods like [18]. Results can be seen in Figure 8.

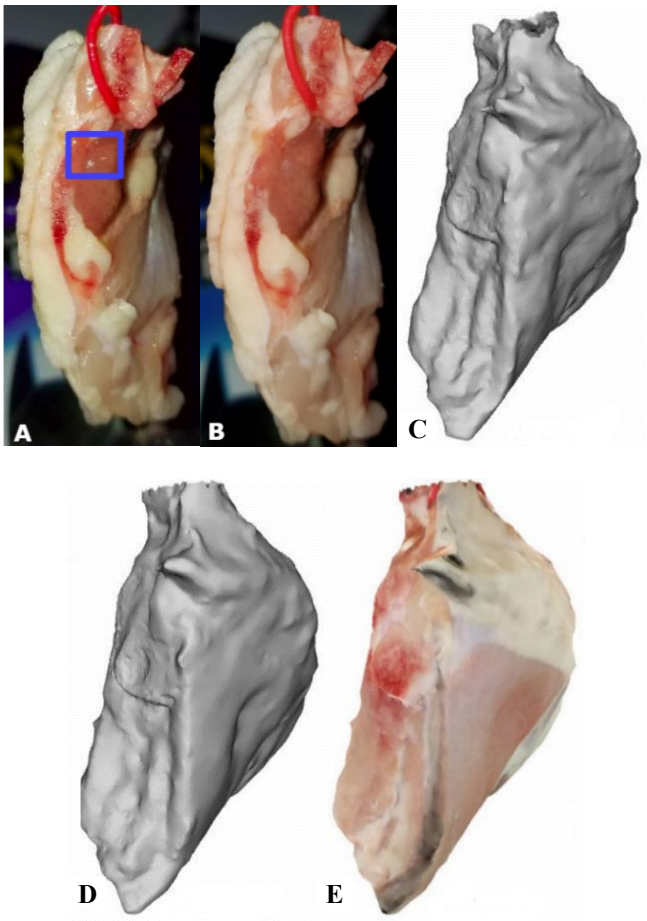

Fig. 8: (A) Original poultry dataset image. (B) Proposed method image – Specular highlights removed. (C) 3D mesh created via contemporary method [18] (D) 3D mesh created via the proposed method. (E) Final 3D reconstruction via the proposed method.

Endoscopy Video Proximal Antrum Dataset: A lesion at the proximal antrum region of the stomach was chosen. This video has most of the common artifacts and complicated scenarios found in endoscopic videos and provided that this 3D reconstruction was created from only 47 images which were not very far apart in terms of camera pose. Results can be seen in Figure 9.

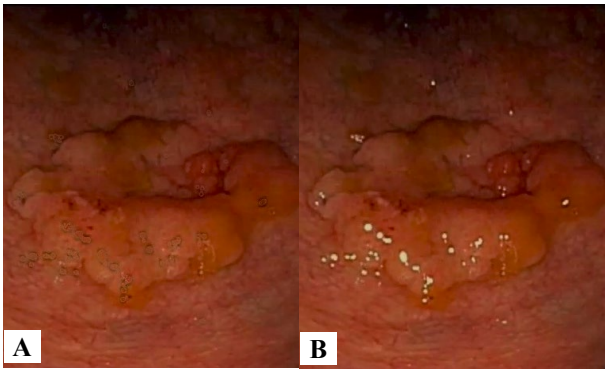

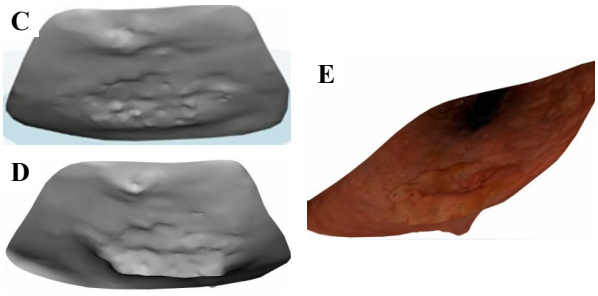

Fig. 9: (A) Original Endoscopy video frame. (B) Proposed method frame – Specular highlights removed. (C) 3D mesh created via contemporary method [18] (D) 3D mesh created via the proposed method. (E) Final 3D reconstruction via the proposed method

VI. Conclusion

This paper presents a reliable and robust specular reflection removal method for 3D tissue reconstruction. One of the primary claims of this method is the complete removal of specular highlights with a zero-magnitude diffused reflection component. A novel patch reconstruction technique was introduced that would reconstruct the missing image information in a way that descriptors of the corresponding local features do not produce a false match between an image pair having a scene overlap. This produces a more accurate 3D reconstruction resilient to specular highlights in terms of 3D model and texture reconstruction. Experiments show superior accuracy for the proposed method in terms of highlight removal and 3D reconstruction compared to contemporary methods.

Acknowledgment

This project was made possible by the Arkansas INBRE program, supported by a grant from the National Institute of General Medical Sciences, (NIGMS), P20 GM103429 from the National Institutes of Health (NIH). This project was also supported by NIH/ NIBIB 1R01EB033674-01A1, 5R01EB025241-04, 3R01EB005807-09A1S1, and 5R01EB005807-10.

References

[1] R. Koch, M. Pollefeys, and L. Van Gool, “Realistic surface reconstruction of 3D scenes from uncalibrated image sequences,” J. Vis. Comput. Animat., vol. 11, no. T. Bergen and T. M. Wittenberg, “Stitching and Surface Reconstruction from Endoscopic Image Sequences: A Review of Applications and Methods,” IEEE J. Biomed. Heal. informatics 2194, 1–20 (2014).

[2] L. Maier-Hein, P. Mountney, a. Bartoli, H. Elhawary, D. Elson, a. Groch, a. Kolb, M. Rodrigues, J. Sorger, S. Speidel, and D. Stoyanov, “Optical techniques for 3D surface reconstruction in computer-assisted laparoscopic surgery,” Med. Image Anal. 17, 974–996 (2013). 3, pp. 115–127, 2000.D. Nistér, O. Naroditsky, and J. Bergen. Visual odometry. In Proceedings of the IEEE Conference on Computer Vision and Pattern Recognition (CVPR), 2004.

[3] X. Sun, Y. Liu, X. Yu, H. Wu, and N. Zhang, “Three-dimensional measurement for specular reflection surface based on reflection component separation and priority

region filling theory," Sensors (Switzerland), vol. 17, no. 1, 2017.
[4] Zhang, Yj. "Advances in Image and Video Segmentation," N.p., 2006. Web.
[5] D. Stoyanov, M. V. Scarzanella, and P. Pratt, "Real-Time Stereo Reconstruction in Robotically Assisted Minimally Invasive Surgery," pp. 275–282, 2010.
[6] Morel, O. (2013). Shape from polarization in Laparoscopy. Sergio E. Martinez Herrera Abed Malti Adrien Bartoli e d ´ Auvergne , Clermont-Ferrand , France Le2i , UMR CNRS 6306 , Universit ´ e de Bourgogne , Le Creusot , France, 1400–1403.
[7] Azevedo, L., Faustino, A. M. R., & Tavares, J. M. R. S. (2015). Segmentation and 3D Reconstruction of Animal Tissues in Histological Images. In Lecture Notes in Computational Vision and Biomechanics (Vol. 21, pp. 193–207). http://doi.org/10.1007/978-3-319-15799-3_14
[8] J. L. Pech-Pacheco, G. Cristobal, J. Chamorro-Martinez, and J. Fernandez-Valdivia, "Diatom auto-focusing in bright-field microscopy: a comparative study," IEEE, vol. 6. pp. 314–317, 2000.
[9] A. Santos and C. O. De Solorzano, "Evaluation of autofocus functions in molecular cytogenetic analysis," J. Microsc., Vol. 188, no. Pt 3, pp. 264–72, 1997.
[10] A. Pretto, E. Menegatti, M. Bennewitz, W. Burgard, and E. Pagello, "A visual odometry framework robust to motion blur," in 2009 IEEE International Conference on Robotics and Automation, 2009, pp. 2250–2257.
[11] H. Zhao, Y. Liu, X. Xie, Y. Liao, and X. Liu, "Filtering Based Adaptive Visual Odometry Sensor Framework Robust to Blurred Images," Sensors, vol. 16, no. 7, p. 1040, Jul. 2016.
[12] A. Ben-Hamadou, C. Daul, C. Soussen, A. Rekik, and W. Blondel, "A novel 3D surface construction approach: Appliciation to 3D endoscopic data," Conf Proc IEEE Image Proc pp. 4425–4428 (2010).
[13] J. Penne, K. Höller, M. Stürmer, T. Schrauder, A. Schneider, R. Engelbrecht, H. Feussner, B. Schmauss, and J. Hornegger, "Time-of-Flight 3-D endoscopy," Med. Image Comput. Comput. Assist. Interv. 12, 467–474 (2009).
[14] M. Agenant, H.-J. Noordmans, W. Koomen, and J. L. H. R. Bosch, "Real-time bladder lesion registration and navigation: a phantom study," PLOS ONE 8, e54348 (2013).
[15] O. G. Grasa, E. Bernal, S. Casado, I. Gil, and J. M. M. Montiel, "Visual slam for handheld monocular endoscope," IEEE Trans. Med. Imaging 33, 135–146 (2014).
[16] M. Hu, G. Penney, M. Figl, P. Edwards, F. Bello, R. Casula, D. Rueckert, and D. Hawkes, "Reconstruction of a 3D surface from video that is robust to missing data and outliers: Application to minimally invasive surgery using stereo and mono endoscopes," Med. Image Anal. 16, 597–611 (2012).
[17] Chow, S.-K., & Chan, K.-L. (2009). Removal of Specular Reflection Component Using Multi-view Images and 3D Object Model (pp. 999–1009). http://doi.org/10.1007/978-3-540-92957-4_87
[18] Tan, P., Lin, S., Quan, L., Shum, H.-Y.: Highlight removal by illuminant-constrained in-painting. In: Proceedings of IEEE International Conference on Computer Vision, pp. 164–169 (2003)
[19] Soper, T. D., Porter, M. P., & Seibel, E. J. (2012). Surface Mosaics of the Bladder Reconstructed From Endoscopic Video for Automated Surveillance. IEEE Transactions on Biomedical Engineering, 59(6), 1670–1680. http://doi.org/10.1109/TBME.2012.2191783
[20] Yoon, K. J., & Kweon, I. S. (2006). Correspondence search in the presence of specular highlights using specular-free two-band images. Lecture Notes in Computer Science (Including Subseries Lecture Notes in Artificial Intelligence and Lecture Notes in Bioinformatics), 3852 LNCS, 761–770. https://doi.org/10.1007/11612704_76
[21] Yang, Q., Tang, J., & Ahuja, N. (2015). Efficient and robust specular highlight removal. IEEE Transactions on Pattern Analysis and Machine Intelligence, 37(6), 1304–1311. https://doi.org/10.1109/TPAMI.2014.2360402
[22] Tan, R., & Ikeuchi, K. (2008). Separating reflection components of textured surfaces using a single image. Digitally Archiving Cultural Objects, 27(2), 353–384. Retrieved from papers://8777af81-a8f3-4573-8f50-d027914805b7/Paper/p3465